
Title	Highly dose dependent damping-like spin–orbit torque efficiency in O-implanted Pt
Author(s)	Utkarsh Shashank, Rohit Medwal, Yoji Nakamura, John Rex Mohan, Razia Nongjai, Asokan Kandasami, Rajdeep Singh Rawat, Hironori Asada, Surbhi Gupta and Yasuhiro Fukuma

Copyright © 2021 AIP Publishing

This is the published version of the following article:

Utkarsh Shashank , Rohit Medwal, Nakamura, Y., Mohan, J. R., Razia Nongjai, Asokan Kandasami, Rawat, R. S., Asada, H., Surbhi Gupta, & Fukuma, Y. (2021). Highly dose dependent damping-like spin–orbit torque efficiency in O-implanted Pt. *Applied Physics Letters*, 118, Article 252406. <https://doi.org/10.1063/5.0054779>

Highly dose dependent damping-like spin-orbit torque efficiency in O-implanted Pt

Utkarsh Shashank¹, Rohit Medwal², Yoji Nakamura¹, John Rex Mohan¹, Razia Nongjai³, Asokan Kandasami³, Rajdeep Singh Rawat², Hironori Asada⁴, Surbhi Gupta^{1,2a)} and Yasuhiro Fukuma^{1,5a)}

¹Department of Physics and Information Technology, Faculty of Computer Science and System Engineering, Kyushu Institute of Technology, 680-4 Kawazu, Iizuka 820-8502, Japan

²Natural Sciences and Science Education, National Institute of Education, Nanyang Technological University 637616, Singapore

³Materials Science Division, Inter University Accelerator Centre, Aruna Asaf Ali Marg, New Delhi 110067, India

⁴Graduate School of Sciences and Technology for Innovation, Yamaguchi University, 2-16-1 Tokiwadai, Ube 755-8611, Japan

⁵Research Center for Neuromorphic AI hardware, Kyushu Institute of Technology, Kitakyushu 808-0196, Japan

^{a)}Author to whom correspondence should be addressed: fukuma@cse.kyutech.ac.jp,
surbhi.gupta@nie.edu.sg

ABSTRACT

Damping-like torque (DLT) arising from the spin Hall effect (SHE) in heavy metals and their alloys has been widely explored for applications in spin-orbit torque MRAM, auto-oscillations, spin waves and domain wall motion. In conventional materials, DLT efficiency is limited by intrinsic properties, while attaining strong spin-orbit coupling and higher spin-charge interconversion, with no compromise to electric properties, are the need of the hour. In this letter, we report the increase of more than 250% in DLT efficiency, θ_{DL} , of modified Pt-oxide, by employing new approach of low energy 20 keV O⁺ ion implantation. Highest fluence of O⁺ implantation (1×10^{17} ions cm⁻²) in Pt enhanced the DLT efficiency from 0.064 to 0.230 and improved the spin transmission for a small trade-off in the longitudinal resistivity (ρ_{Pt} to $\rho_{Pt-Oxide}$) from 55.4 to 159.5 $\mu\Omega$ -cm respectively. The linear increase in the transverse spin Hall resistivity ρ_{SH} with the square of the longitudinal resistivity from impurities ρ_{imp} , as the composition changes, i.e. the observation of $\rho_{SH}^{imp} \propto \rho_{imp}^2$ behavior, suggests a side-jump mechanism for the enhanced SHE in O-implanted Pt. Further, no break in two-fold and mirror symmetry of torques from O-implanted Pt allows the use of spin-torque ferromagnetic resonance (ST-FMR) based lineshape analysis to quantify such torques.

The existence of a strong spin-orbit coupling (SOC) in heavy metal (HM) has been instrumental in the research based on spin-based memory and logic devices¹⁻³. The high SOC is utilized to generate large spin current density (J_S) converted from charge current density (J_C) in HM by means of phenomenological spin Hall effect (SHE)⁴. This spin current exerts a spin-orbit torque (SOT) on the magnetization of the adjacent ferromagnet (FM) layer attached to HM, which is one of the most important feature of SHE^{5,6}. There are two basic components of SOT, first being the damping-like torque (DLT) $\vec{\tau}_{DL} \propto \hat{m} \times (\hat{\sigma} \times \hat{m})$, and second is the field-like torque (FLT) $\vec{\tau}_{FL} \propto -(\hat{\sigma} \times \hat{m})$ ^{7,8}, where $\hat{\sigma}$ is the unit vector along the spin polarization direction of the spin current, and \hat{m} is the magnetization unit vector. In fact, the former is more critical than the latter considering the intriguing applications that it provides in SOT-MRAM, logic operations, auto-oscillations, spin waves transmission and domain wall motion^{2,9,10}.

The possibility of a strong DLT from the pre-existing heavy metals has attracted various groups to enhance it even further by alloying with not only metals such as PtSn alloy¹¹, Zn and Ni-doped Pt¹², Cu-Pt alloy¹³, Pt-Pd Alloy¹⁴ Pt-Au alloy¹⁵ etc. but the insertion of lighter elements like oxidation of Pt¹⁶, Ta¹⁷, W¹⁸ and even recently adding nitrogen in Pt¹⁹ have been shown as successful approaches to improve the charge-spin interconversion efficiency. However, for oxidation, most of the incorporation in these materials is attained from the natural process of sputtering which, if not controlled artificially such as alloying or other methods, may not be monotonic in DLT with varying concentrations^{17,19}. Hence, in this respect, ion implantation, being an established artificial material engineering technique in the semiconductor industry is much more useful to incorporate non-metallic elements in heavy metals to enhance the DLT further. As a matter of fact, ion implantation or ion irradiation is already taking huge strides in the designing of future generation spintronic devices such as in spin-torque nano-oscillator using He⁺

irradiation²⁰, interfacial hydrogen and oxygen ion manipulation at CoFeB/MgO based magnetic tunneling junction structures²¹, SOT driven multi-level switching in He⁺ irradiated W/CoFeB/MgO hall bars²² etc. To add, we had previously designed a new spin Hall material (SHM) by implanting low energy 12 keV sulfur ions in prototype Pt which demonstrated eight-times enhanced charge-to-spin interconversion efficiency and very large spin Hall conductivity of $\sim 8.32 \times 10^5 \left(\frac{\hbar}{2e}\right) \Omega^{-1} \text{m}^{-1}$ at 10 K, highest among reported Pt and its derivatives²³.

In this paper, we report high DLT efficiency attained in modified Pt/NiFe, fabricated by non-metallic oxygen ion implantation, at low energy of 20 keV with varying fluence/dose of $2 \times 10^{16} - 1 \times 10^{17}$ ions cm^{-2} . We find consistent dose-dependent enhancement in DLT efficiency, θ_{DL} , which is more than 250% and improved spin transmission estimated using room temperature spin-torque ferromagnetic resonance (ST-FMR)²⁴ based line shape analysis (spectral analysis) and linewidth analysis (modulation of damping) measurements. The linear increase in the impurity induced SH resistivity $\rho_{\text{SH}}^{\text{imp}}$ with square of the longitudinal resistivity $(\rho_{\text{Pt-Oxide}} - \rho_{\text{Pt}})^2$ reveals a side-jump scattering as the dominant mechanism of the enhanced SHE. In addition, no breaking of the mirror and two-fold symmetry in exerted spin-orbit torques shows bulk-SHE driven enhanced charge-spin interconversion. Compared with pristine Pt and other reported heavy metal oxide systems, O-implanted Pt/NiFe bilayer exhibited high $\theta_{\text{DL}} = 0.230$ and spin mixing conductance $g_{\text{eff}}^{\uparrow\downarrow} = 2.048 \times 10^{19} \text{m}^{-2}$ with minor compromise in longitudinal resistivity. Our results open up new avenues for ion-implantation as a novel guiding approach to design advanced materials that cater to low-power energy-efficient devices based on spin-orbitronics.

The multilayer stack of Pt (10 nm)/MgO(10 nm)/Al₂O₃ (10 nm) on Si/SiO₂ substrates were deposited at room temperature using ultrahigh vacuum sputtering. Then, samples were implanted

with 20 keV O-ion beam at a dose/fluence of 2×10^{16} ions cm^{-2} , 5×10^{16} ions cm^{-2} , and 1×10^{17} ions cm^{-2} respectively. Then, oxide capping layers of MgO and Al₂O₃ were removed by Ar⁺ ion milling. One batch of samples was used for microstructure and surface morphology investigations. Supplementary figure S1(a-c) depict the microstructure image of respective O-implanted Pt surfaces using the scanning electron microscope (SEM) and affirm no substantial surface damage on any of the samples exposed to respective ion fluences of 2×10^{16} ions cm^{-2} , 5×10^{16} ions cm^{-2} , and 1×10^{17} ions cm^{-2} . The average root-mean-square roughness was determined to be varying only from $(0.76 - 0.96) \pm 0.01$ nm from respective topography image analysis. So, these results indicate that the optimized oxide capping layer provided the necessary protection and led to minimal surface agitation of 10 nm thick Pt films, and thus were suitable for device fabrication. We used the second batch to deposit top NiFe (5 nm) layer using ultrahigh vacuum sputtering immediately after the Ar⁺-milling process. Using photolithography, all three bilayer samples (named as N1, N2, and N3 with implanted doses of 2×10^{16} ions cm^{-2} , 5×10^{16} ions cm^{-2} , and 1×10^{17} ions cm^{-2} respectively) were then patterned into $10 \times 65 \mu\text{m}^2$ long micro strips. Finally, Ti (10nm)/Al (200 nm) electrodes were deposited using a lift-off process to design the co-planar waveguide structure for ST-FMR measurements as shown by optical image in Figure 1(a). Similarly, Hall bars were also fabricated to determine longitudinal resistivity $\rho_{\text{Pt-oxide}}$ of different O⁺-dose implanted Pt without top NiFe layer.

First, to determine the DLT efficiency θ_{DL} , we performed the lineshape analysis which uses the ratio of symmetric and antisymmetric components of ST-FMR spectra to calculate θ_{DL} . The schematic of the ST-FMR measurement set-up is shown in Fig. 1(a). The device was excited with a microwave current I_{rf} of varying frequency f (5-11 GHz) with an applied power of $P_{\text{app}} = 10$ dBm (10 mW). Simultaneously, in-plane magnetic field H_{ext} , was also swept from -2000 Oe to

+2000 Oe at an angle of $\phi = 45^\circ$ with respect to device length. Thereby, flowing J_C in O-implanted Pt gets converted into J_S due to SHE and exerts DLT on the magnetization of adjacent FM layer. Meanwhile, h_{rf} arising from I_{rf} exerts an Oersted field torque (OFT) (Ampere's Law) and both torques together drive magnetization precession in the NiFe layer. At FMR conditions, the mixing of periodic change in magnetoresistance ΔR of NiFe and I_{rf} produces a rectified DC voltage V_{mix} which is detected using a lockin amplifier²⁴. Figure 1 (b-d) (i) shows the typical ST-FMR spectra for N1, N2, and N3 respectively measured in the applied microwave frequency range 5-11 GHz. Note that, there is a reversal of symmetric component with the reverse in polarity of external magnetic field (H_{ext}) which agrees with SHE symmetry and it also rules out the possibility of non-controlled relative phase between I_{rf} and h_{rf} that we retained in present measurements for wide frequency range²⁵. In addition, we also performed the calibration of P_{app} dependence of ST-FMR signal, provided in supplementary section S2. As applied power increased from 0 dBm (1 mW) to 11 dBm (12.58 mW), the increased V_{mix} signal exhibited no change in spectral linewidth and resonance field position which indicated that precessing magnetization was in the linear regime at chosen power $P_{app} = 10$ dBm (10mW). Next figure 1 (b-d) (ii) shows the ST-FMR spectrum obtained at $f = 5$ GHz respectively for N1, N2, and N3 sample which are then subsequently fitted using:

$$V_{mix} = SF_{sym}(H_{ext}) + AF_{asym}(H_{ext}), \quad (1)$$

where, $F_{sym}(H_{ext}) = \frac{(\Delta H)^2}{(H_{ext}-H_0)^2+(\Delta H)^2}$ is the symmetric component with weight S, and

$F_{asym}(H_{ext}) = \frac{\Delta H(H_{ext}-H_0)}{(H_{ext}-H_0)^2+(\Delta H)^2}$ is the antisymmetric component with weight A and ΔH and H_0 are

the half-width-at-half-maximum and resonance field of FMR spectra²⁴. While the symmetric component is proportional to DLT, the antisymmetric component is proportional to OFT²³. The

V_{mix} spectrum is de-convoluted into symmetric and antisymmetric components for N1, N2, and N3 samples. It can be noticed that there is an increase in the symmetric component as the dosage of oxygen ions increases 5 times which implies a linear increase in DLT with dosage.

Furthermore, ΔH was plotted as a function of applied frequency f in Fig. 2(a), for N1, N2, and N3. The Gilbert damping parameter α was estimated using:

$$\Delta H = \Delta H_0 + \frac{2\pi\alpha}{\gamma} f, \quad (2)$$

where the first term ΔH_0 is the inhomogeneous linewidth broadening and γ is the gyromagnetic ratio. Here, α was found to be increasing with dose for O-implanted Pt, N1 (0.0137), N2 (0.0153) and N3 (0.0164), unlike to Ta(O)/Py¹⁷ which showed small deviation around average ~ 0.01 for different oxygen flow rates in Ta. Important to notice, that the inhomogeneous linewidth $\Delta H_0 \sim 5$ Oe in all cases was found to very small which further confirmed the smooth and high quality of O-implanted Pt/NiFe interface fabrication. Dose dependent increase in α clearly dictates the effect of enhanced DLT from O-implanted Pt. However, the additional spin relaxation due the presence of spin pumping cannot be ruled out here. Further, spin pumping also contributes to symmetric component of the rectified V_{mix} signal in ST-FMR measurements²⁶. Therefore, to confirm that the symmetric part is dominantly proportional to DLT here, the spin pumping contribution, V_{sp} (see supplementary section S3) was estimated and found it to be ~ 1 % only. It showed that spin current pumping back into the O-implanted Pt layer from precessing NiFe was negligible.

The effective magnetization $4\pi M_{\text{eff}}$ values were then extracted by fitting the resonance frequency f as a function of H_0 in Fig. 2(b) using the Kittel formula due to the negligibly small in-plane magnetic anisotropy in N1, N2 and N3 sample using:

$$f = \frac{\gamma}{2\pi} \sqrt{H_o(H_o + 4\pi M_{\text{eff}})}, \quad (3)$$

The effective magnetization $4\pi M_{\text{eff}}$ was calculated to be 0.799 T, 0.800 T and 0.811 T for N1, N2, and N3 respectively. We also evaluated the spin mixing conductance $g_{\text{eff}}^{\uparrow\downarrow}$ ²⁷ which is an important parameter describing the absorption of transverse spin current which is influenced by HM/FM interface. There is an enhancement of $g_{\text{eff}}^{\uparrow\downarrow}$ with dose from $1.534 \times 10^{19} \text{ m}^{-2}$ (N1) to $2.048 \times 10^{19} \text{ m}^{-2}$ (N3). So, after confirming the insignificant contribution of spin pumping in symmetric component of the spectra, we proceeded to quantify DLT efficiency θ_{DL} , given as²⁴:

$$\theta_{\text{DL}}^{\text{LS}} = \frac{S}{A} \frac{e\mu_o M_s t d}{\hbar} \sqrt{1 + \frac{4\pi M_{\text{eff}}}{H_o}}, \quad (4)$$

where, e is the electron charge, μ_o is the permeability of free space, t is thickness of NiFe layer, d is thickness of Pt-Oxide layer, M_s is the saturation magnetization of NiFe. Figure 2(c) shows the calculated value of $\theta_{\text{DL}}^{\text{LS}}$ of 0.075 ± 0.002 , 0.107 ± 0.002 and 0.230 ± 0.003 for N1, N2, and N3 respectively. This monotonic increase of $\theta_{\text{DL}}^{\text{LS}}$ with O-dose shows that ion implantation could be a better alternative to incorporate nonmetallic elements in transition metals when compared to incorporating oxides/nitrides via sputtering^{17,19}. In particular, the lineshape analysis performed here only at an angle of $\phi = 45^\circ$ may not reveal the complete visualization of the generated spin-orbit torques²⁸ and therefore, angular ST-FMR measurements by varying the H_{ext} from $\phi = 0^\circ$ to 360° is also crucial to analyze. Figure 2(d) shows that both S and A component are well fitted with expected $\sin 2\phi \cos \phi$ behavior for highest dose of $1 \times 10^{17} \text{ ions cm}^{-2}$ implanted Pt-Oxide/NiFe (N3) sample with no breaking of mirror and two-fold symmetry²⁹. It implies that lineshape analysis can be used for O-implanted Pt system which could give it an edge over other transition-metal dichalcogenides²⁹, where broken symmetry needs complex analysis to quantify such torques.

Please refer supplementary section S4 to see the angular dependence of spin-orbit torques in other O-implanted Pt samples N1 and N2.

Second, to make the estimation of DLT efficiency, θ_{DL} , more comprehensive, we employed an alternative approach of linewidth modulation as well since this method is free from spin pumping³⁰. We used DC-biased ST-FMR technique in which an additional DC current I_{dc} (+/-0.8mA) was also applied along with I_{rf} to modulate the linewidth ΔH which either get increased or decreased based on the polarity of applied H_{ext} . The change in ΔH can be seen in Fig. 3(a-c) for N1, N2 and N3 respectively which explicitly increased from ~ 1 Oe (N1) to ~ 1.7 Oe (N2) and finally to ~ 3 Oe (N3). Further, using this change in ΔH , we evaluated θ_{DL} using the equation³¹:

$$\theta_{DL}^{LW} = \frac{\frac{2e}{\hbar} \left(H_0 + \frac{M_{eff}}{2} \right) \mu_0 M_s t \left| \frac{\Delta \alpha_{eff}}{\Delta J_C} \right|}{\sin \phi}, \quad (5)$$

where, $\Delta \alpha_{eff}$ is the effective change in damping due to I_{dc} . In accordance with the lineshape analysis, we observed a similar trend where θ_{DL}^{LW} increased monotonically from 0.074 ± 0.021 for N1 to 0.106 ± 0.022 for N2 and then finally to 0.231 ± 0.024 for N3.. The DLT efficiency values obtained from lineshape and linewidth modulation analyses along with estimated $g_{eff}^{\uparrow\downarrow}$ and $\rho_{Pt-Oxide}$ values are summarized in Table 1. Essentially by changing the impurity concentration i.e. different O-implantation dose in much wider range, we could obtain highly dose dependent DLT efficiency and therefore, it is more likely to be caused by extrinsic mechanism.

As we understand there are two types of mechanism of extrinsic SHE namely, the skew scattering governed by explicit behavior of SH resistivity (ρ_{SH}^{imp}) proportional to impurity induced resistivity (ρ_{imp}), while, the side jumping scattering is associated with $\rho_{SH}^{imp} \propto \rho_{imp}^2$ relationship when impurities are the only source of resistivity³². We found a monotonic dependence of θ_{DL}

with the increase in longitudinal resistivity $\rho_{\text{Pt-Oxide}}$ as concentration of O^+ implantation increased as shown in Fig. 4, it hints towards the side-jump mechanism as the dominant origin of the enhanced SHE. To further probe the explicit contribution of impurities, we next focused on $\rho_{\text{SH}}^{\text{imp}} = \rho_{\text{SH}}^{\text{Pt-Oxide}} - \rho_{\text{SH}}^{\text{Pt}}$ where $\rho_{\text{SH}}^{\text{Pt-Oxide}}$ and $\rho_{\text{SH}}^{\text{Pt}}$ are the SH resistivity of Pt-Oxide and pristine Pt which were estimated from respective charge-spin interconversion efficiency. See supplementary note S5 showing DLT efficiency obtained for pristine N0: Pt/NiFe sample. Here, the longitudinal resistivity from impurities ρ_{imp} , is identified using $\rho_{\text{imp}} = \rho_{\text{Pt-Oxide}} - \rho_{\text{Pt}}$ and prominent signature of linear trend in $\rho_{\text{SH}}^{\text{imp}}$ vs ρ_{imp}^2 plot (see in inset of Fig. 4) establishes the extrinsic side-jump as the main origin of 250% enhanced SHE in O-implanted Pt with very small trade-off in longitudinal resistivity from 55.4 to 159.5 $\mu\Omega\text{-cm}$. For comparison, L. Yang et. al., obtained comparative θ_{DL} of ~ -0.30 with $\rho_{\text{Ta(O)}}$ of $\sim 200 \mu\Omega\text{-cm}^{17}$ and E. Sagasta et. al., obtained a θ_{DL} of ~ -0.15 with a $\rho_{\text{Ta(N)}}$ of $\sim 3000 \mu\Omega\text{-cm}^{33}$, which highlights the present O-implanted Pt as more promising material for spintronic applications using DLT.

In summary, we demonstrated a simple and effective implantation method that promotes the extrinsic spin Hall effect in a Pt layer to significantly enhance the room temperature damping-like-torque efficiency by more than 250%. The highest O^+ ion implantation of 1×10^{17} ions cm^{-2} fluence at optimized energy of 20 keV in Pt led to very high damping-like-torque $\theta_{\text{DL}} = 0.230$, which is much larger than the control sample of pristine Pt ($\theta_{\text{DL}} = 0.064$). Both spectral line shape and modulation of damping in ST-FMR measurements unveiled the highly dose dependent increase in θ_{DL} with improved spin transmission. Furthermore, linear fit of $\rho_{\text{SH}}^{\text{imp}}$ vs ρ_{imp}^2 plot, highlights the side-jump scattering as dominant mechanism of the enhanced SHE in our samples.

Our results emphasize on the ability to efficiently interconvert spin into electrical currents via custom engineered ion implantation.

ACKNOWLEDGEMENTS

U.S. would like to acknowledge the Kanazawa Memorial Foundation Scholarship. Y.F. and H.A. would like to acknowledge JSPS Grant-in-Aid (KAKENHI No. 18H01862 and 19K21112). R.M., S.G. and R.S.R. would like to acknowledge research grants MOE2017-T2-2-129, CRP21-2018-0093, and MOE2019-T2-1-058. The authors thank Mr. Raj Kumar, IUAC for his support in oxygen ion implantations.

DATA AVAILABILITY

The data that support the findings of this study are available from the corresponding author upon reasonable request.

REFERENCES

- ¹ L. Liu, O.J Lee, T. J. Gudmundsen, D. C. Ralph, and R. A. Burhman, Phys. Rev. Lett. **109**, 096602 (2012). <https://doi.org/10.1103/PhysRevLett.109.096602>
- ² A. Manchon, J. Železný, I. M. Miron, T. Jungwirth, J. Sinova, A. Thiaville, K. Garello, and P. Gambardella, Rev. Mod. Phys. **91**, 035004 (2019).
<https://doi.org/10.1103/RevModPhys.91.035004>
- ³ A. Soumyanarayanan, N. Reyren, A. Fert, and C. Panagopoulos, Nature, **539**, 509 (2016).
<https://doi.org/10.1038/nature19820>
- ⁴ J. E. Hirsch, Phys. Rev. Lett. **83**, 1834 (1999).
<https://doi.org/10.1103/PhysRevLett.83.1834>
- ⁵ L. Liu, C.-F. Pai, Y. Li, H. W. Tseng, D.C. Ralph, and R.A. Burhman, Science **336**, 555 (2012). <https://doi.org/10.1126/science.1218197>
- ⁶ S. Emori, U. Bauer, S. M. Ahn, E. Martinez, and G. S. D. Beach, Nat. Mater. **12**, 611 (2013). <https://doi.org/10.1038/nmat3675>
- ⁷ W. Zhang, W. Han, X. Jiang, S. –H. Yang, and S. S. P. Parkin, Nat. Phys. **11**, 496 (2015).
<https://doi.org/10.1038/nphys3304>
- ⁸ H. Kurebayashi, J. Sinova, D. Fang, A. C. Irvine, T. D. Skinner, J. Wunderlich, V. Novák, R. P. Campion, B. L. Gallagher, E. K. Vehstedt, L. P. Zârbo, K. Výborný, A. J. Ferguson, and T. Jungwirth, Nat. Nanotechnol. **9**, 211 (2014).
<https://doi.org/10.1038/nnano.2014.15>
- ⁹ J.Ryu. S. Lee, K. J. Lee, and B. G. Park, Adv. Mater. **32**, 1907148 (2020).
<https://doi.org/10.1002/adma.201907148>
- ¹⁰ B. Divinsky, V. E. Demidov, S. Urazdin, R. Freeman, A. N. Rinkevich, and S.O Demokritov, Adv. Mater. **30**, 1802837 (2018). <https://doi.org/10.1002/adma.201802837>
- ¹¹ M. Li, L. Jin, Y. H. Rao, Z. Zhong, X. Tang, B. Liu, H. Meng, Q. Yang, Y. Lin, and H. Zhang, Journal of Mag. and Magn. Mater. **507**, 166860 (2020).
<https://doi.org/10.1016/j.jmmm.2020.166860>
- ¹² W. Iwamoto, T. Yamamoto, K. Tsuchii, Y. Tazaki, A. Asami, H. Hayashi, Y. Einaga, and K. Ando, ACS Appl. Electron. Mater. **2**, 2098 (2020).
<https://doi.org/10.1021/acsaelm.0c00330>

- ¹³ G. D. H. Wong, W. C. Law, F. N. Tan, W. L. Gan, C. C. I. Ang, Z. Xu, C. S. Seet, and W. S. Lew, *Sci. Rep.* **10**, 9631 (2020). <https://doi.org/10.1038/s41598-020-66762-8>
- ¹⁴ X. Zhou, M. Tang, X. L. Fan, X. P. Qiu, and S. M. Zhou, *Phys. Rev. B* **94**, 144427 (2016). <https://doi.org/10.1103/PhysRevB.94.144427>
- ¹⁵ L. Zhu, D. C. Ralph, and R. A. Burhman, *Phys. Rev. Appl.* **10**, 031001 (2018). <https://doi.org/10.1103/PhysRevApplied.10.031001>
- ¹⁶ H. An, Y. Kanno, A. Asami, and K. Ando, *Phys. Rev. B* **98**, 014401 (2018). <https://doi.org/10.1103/PhysRevB.98.014401>
- ¹⁷ L. Yang, Y. Fei, K. Zhou, L. Chen, Q. Fu, L. Li, C. Yan, H. Li, Y. Du, and R. Liu, *Appl. Phys. Lett.* **118**, 032405, (2021). <https://doi.org/10.1063/5.0033752>
- ¹⁸ K. U. Demasius, T. Phung, W. Zhang, B. P. Hughes, S. H. Yang, A. Kellock, W. Han, A. Pushp, and S. S. P. Parkin, *Nat. Commun.* **7**, 10644 (2016). <https://doi.org/10.1038/ncomms10644>
- ¹⁹ Z. Xu, G. D. H. Wong, J. Tang, E. Liu, W. Gan, F. Xu, and W. S. Lew, *Appl. Phys. Lett.* **118**, 062406 (2021). <https://doi.org/10.1063/5.0035815>
- ²⁰ S. Jiang, R. Khymyn, S. Chung, T. Q. Le, L. H. Diez, A. Houshang, M. Zahedinejad, D. Ravelosona, and J. Åkerman, *Appl. Phys. Lett.* **116**, 072403 (2020). <https://doi.org/10.1063/1.5137837>
- ²¹ W. L. Peng, J. Y. Zhang, G. N. Feng, X. L. Xu, C. Yang, Y. L. Jia, and G. H. Yu, *Appl. Phys. Lett.* **115**, 092402 (2019). <https://doi.org/10.1063/1.5110206>
- ²² X. Zhao, Y. Liu, D. Zhu, M. Sall, X. Zhang, H. Ma, J. Langer, B. Ocker, S. Jaiswal, G. Jakob, M. Kläui, W. Zhao, and D. Ravelosona, *Appl. Phys. Lett.* **116**, 242401 (2020). <https://doi.org/10.1063/5.0010679>
- ²³ U. Shashank, R. Medwal, T. Shibata, R. Nongjai, J. V. Vas, M. Duchamp, K. Asokan, R. S. Rawat, H. Asada, S. Gupta, and Y. Fukuma, *Adv. Quantum Technol.* **4**, 2000112 (2021). <https://doi.org/10.1002/qute.202000112>
- ²⁴ L. Liu, T. Moriyama, D. C. Ralph, and R. A. Burhman, *Phys. Rev. Lett.* **106**, 036601 (2011). <https://doi.org/10.1103/PhysRevLett.106.036601>
- ²⁵ M. Harder, Y. Gui, and C.-M. Hu, *Phys. Rep.* **661**, 1 (2016). <https://doi.org/10.1016/j.physrep.2016.10.002>

- ²⁶ S. Gupta, R. Medwal, D. Kodama, K. Kondou, Y. Otani, and Y. Fukuma, *Appl. Phys. Lett.* **110**, 022404 (2017). <https://doi.org/10.1063/1.4973704>
- ²⁷ R. Medwal, S. Gupta, R. S. Rawat, A. Subramanian, and Y. Fukuma, *Phys. Status Solidi RRL* **13**, 1900267 (2019). <https://doi.org/10.1002/pssr.201900267>
- ²⁸ J. Sklenar, W. Zhang, M. B. Jungfleisch, H. Saglam, S. Grudichak, W. Jiang, J. E. Pearson, J. B. Ketterson, and A. Hoffman, *Phys. Rev. B* **95**, 224431 (2017). <https://doi.org/10.1103/PhysRevB.95.224431>
- ²⁹ D. MacNeill, G. M. Steihl, M. H. D. Guimaraes, R. A. Burhman, J. Park, and D. C. Ralph, *Nat. Phys.* **13**, 300 (2017). <https://doi.org/10.1038/nphys3933>
- ³⁰ A. Okada, Y. Takeuchi, K. Furuya, C. Zhang, H. Sato, S. Fukami, and H. Ohno, *Phys. Rev. Appl.* **12**, 014040 (2019). <https://doi.org/10.1103/PhysRevApplied.12.014040>
- ³¹ T. Nan, S. Emori, C. T. Boone, X. Wang, T. X. Oxholm, J. G. Jones, B. M. Howe, G. J. Brown, and N. X. Sun, *Phys. Rev. B* **91**, 214416 (2015). <https://doi.org/10.1103/PhysRevB.91.214416>
- ³² Y. Niimi, M. Morota, D. H. Wei, C. Deranlot, M. Basletic, A. Hamzic, A. Fert, and Y. Otani, *Phys. Rev. Lett.* **106**, 126601 (2011). <https://doi.org/10.1103/PhysRevLett.106.126601>
- ³³ T.-Y. Chen, C.-T. Wu, H.-W. Yen, and C.-F. Pai, *Phys. Rev. B* **96**, 104434 (2017). <https://doi.org/10.1103/PhysRevB.96.104434>

Figure Captions:

Figure 1. (a) ST-FMR detection technique using lock-in amplifier with optical image of micro-device and thin film structure. (b) Obtained rectified voltage spectra V_{mix} for $f = 5$ to 11 GHz in (b) (i) for N1, in (c) (i) for N2, and in (d) (i) for N3. V_{mix} for $f = 5$ GHz with solid line as fit (using eqn. 1), and with de-convoluted fits of the symmetric and antisymmetric components shown by green and violet solid line respectively in (b) (ii) N1, (c) (ii) N2, and (d) (ii) N3.

Figure 2. (a) ΔH vs f (with solid lines as linear fit), (b) f vs H_0 (with solid lines as Kittel equation fit) and (c) Frequency invariant $\theta_{\text{DL}}^{\text{LS}}$ obtained N1, N2, N3 (d) Angular dependence of symmetric and antisymmetric components in ST-FMR spectra for N3 for $f = 5$ GHz with solid lines fitted by $\sin 2\phi \cos \phi$.

Figure 3. Varying ΔH plotted as a function of I_{dc} (+/- 0.8 mA) for $f = 5$ GHz with slope determined from linear fit (solid lines) for (a) N1, (b) N2, and (c) N3.

Figure 4. θ_{DL} as a function $\rho_{\text{Pt-oxide}}$ for N0 (Pristine Pt), N1, N2, N3. Inset shows $\rho_{\text{SH}}^{\text{imp}}$ vs ρ_{imp}^2 , with solid black line as a linear fit.

Table 1: $g_{\text{eff}}^{\uparrow\downarrow}$, $\theta_{\text{DL}}^{\text{LS}}$, $\theta_{\text{DL}}^{\text{LW}}$, and $\rho_{\text{Pt-oxide}}$ for different dose of oxygen.

O⁺ implantation Dose	Sample	$g_{\text{eff}}^{\uparrow\downarrow}$ (10^{19} m^{-2})	$\theta_{\text{DL}}^{\text{LS}}$	$\theta_{\text{DL}}^{\text{LW}}$	$\rho_{\text{Pt-oxide}}$ ($\mu\Omega\text{-cm}$)
$2 \times 10^{16} \text{ ions cm}^{-2}$	N1	1.534	0.075	0.074	84.9
$5 \times 10^{16} \text{ ions cm}^{-2}$	N2	1.809	0.108	0.106	117.0
$1 \times 10^{17} \text{ ions cm}^{-2}$	N3	2.048	0.230	0.231	159.5

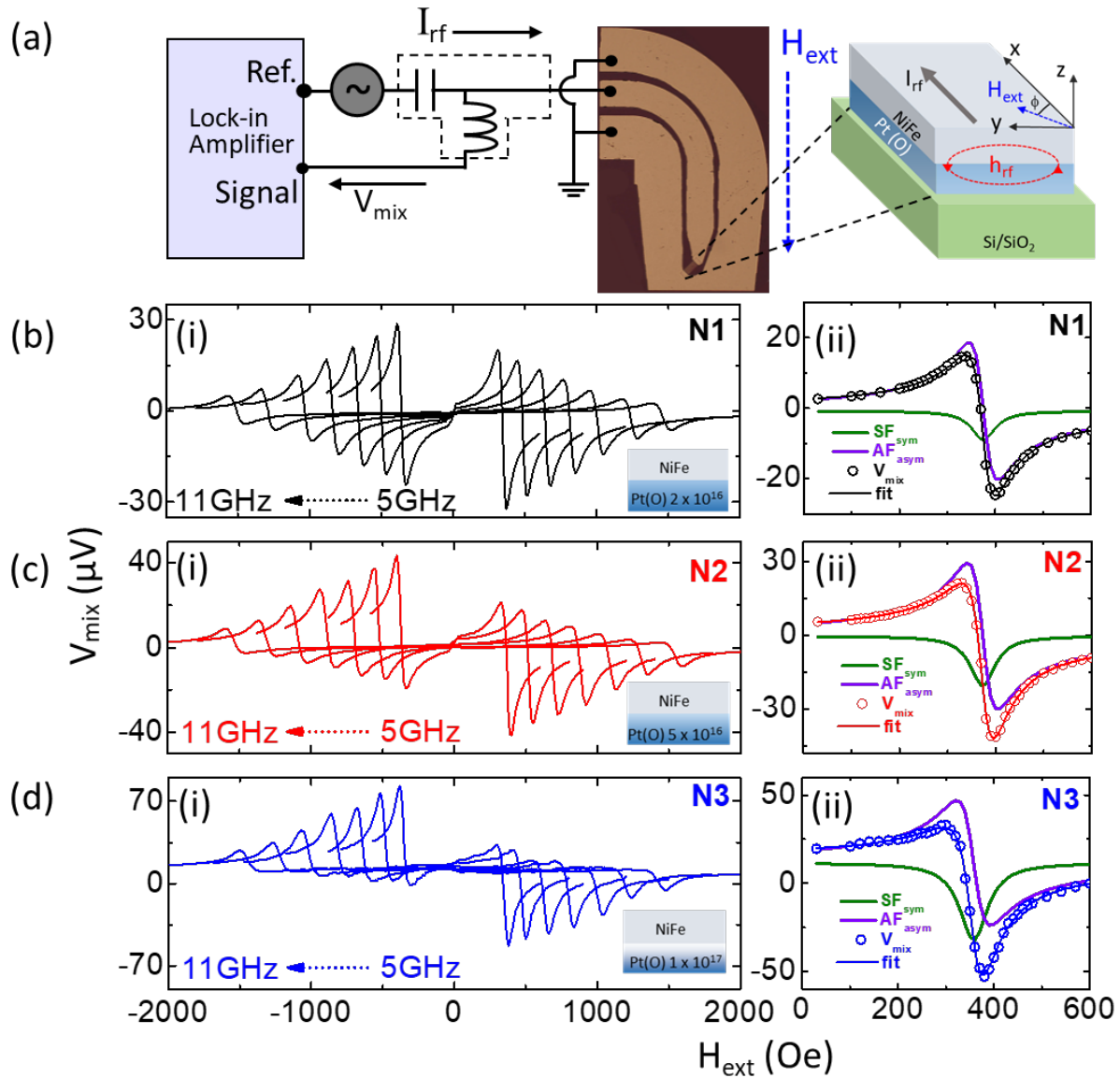


Fig. 1, U. Shashank et al.

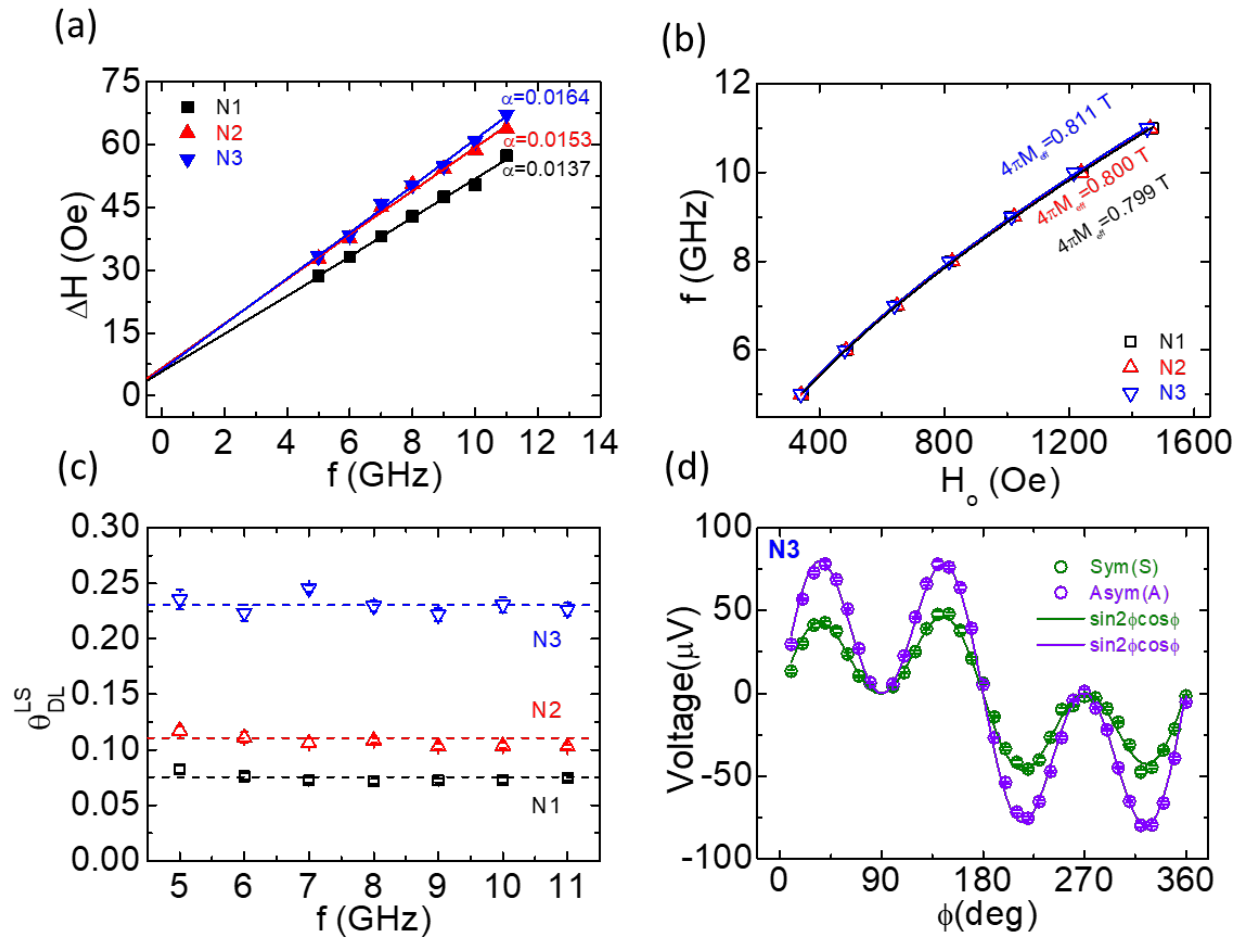


Fig. 2, U. Shashank et al.

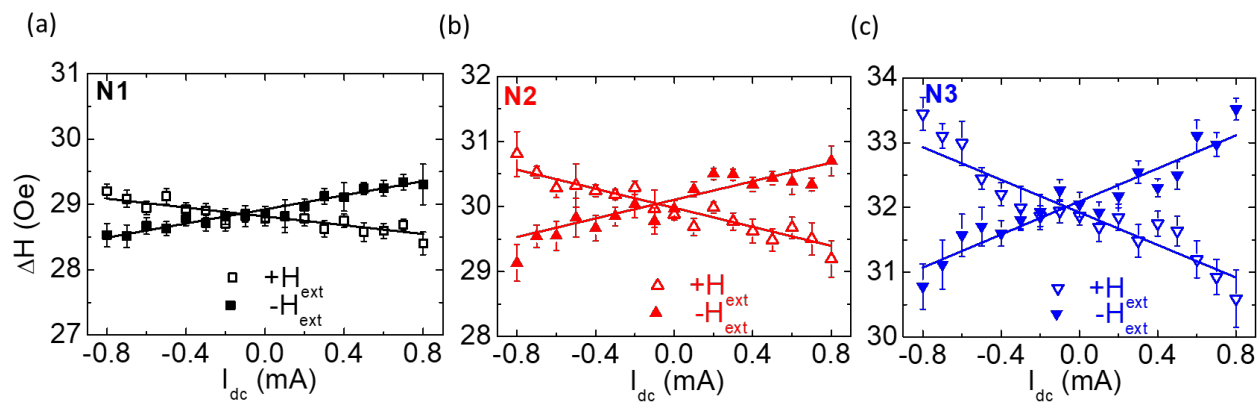


Fig. 3, U. Shashank et al.

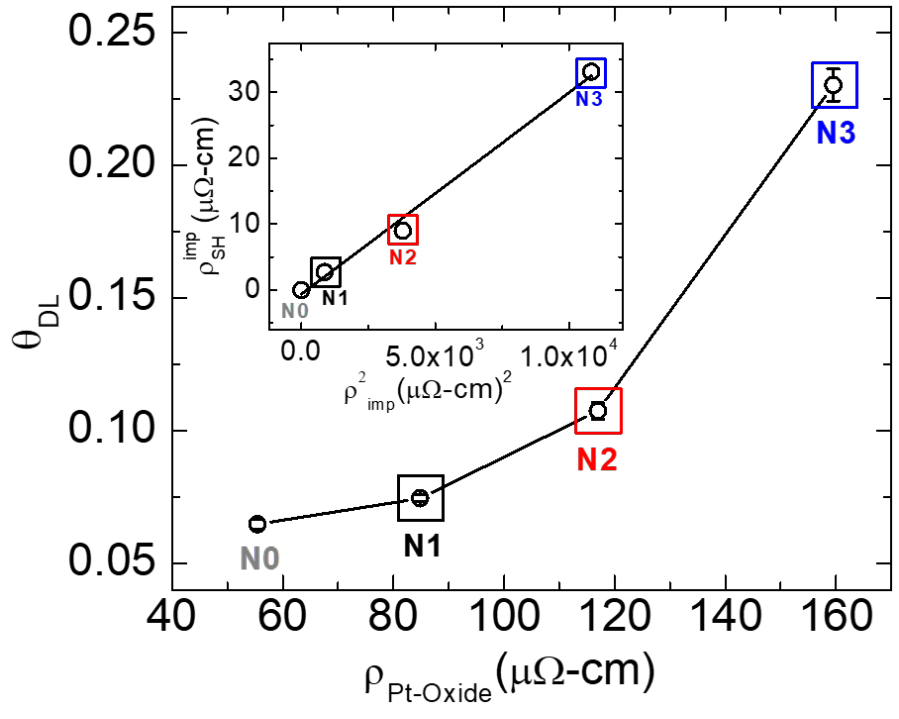


Fig. 4, U. Shashank et al.

Supplementary Information

Highly dose-dependent damping-like spin-orbit torque efficiency in O-implanted Pt

Utkarsh Shashank¹, Rohit Medwal², Yoji Nakamura¹, John Rex Mohan¹, Razia Nongjai³, Asokan Kandasami³, Rajdeep Singh Rawat², Hironori Asada⁴, Surbhi Gupta^{1,2a)} and Yasuhiro Fukuma^{1,5a)}

¹Department of Physics and Information Technology, Faculty of Computer Science and System Engineering, Kyushu Institute of Technology, 680-4 Kawazu, Iizuka 820-8502, Japan

²Natural Sciences and Science Education, National Institute of Education, Nanyang Technological University 637616, Singapore

³Materials Science Division, Inter University Accelerator Centre, Aruna Asaf Ali Marg, New Delhi 110067, India

⁴Graduate School of Sciences and Technology for Innovation, Yamaguchi University, 2-16-1 Tokiwadai, Ube 755-8611, Japan

⁵Research Center for Neuromorphic AI hardware, Kyushu Institute of Technology, Kitakyushu 808-0196, Japan

^{a)}Author to whom correspondence should be addressed: fukuma@cse.kyutech.ac.jp,

surbhi.gupta@nie.edu.sg

Contents:

S1: Microstructure for different doses of O-implanted Pt after removal of capping layers

S2: Microwave power dependence of ST-FMR signal

S3: Role of Spin pumping contribution in the symmetric component of ST-FMR signal

S4: Angular dependent ST-FMR measurements

S5: ST-FMR measurements for pristine Pt/NiFe

S1: Microstructure for different doses of O-implanted Pt after removal of capping layers

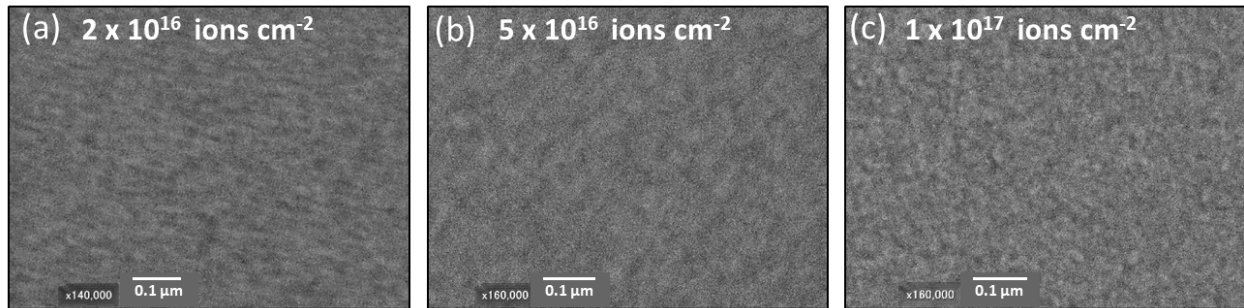


Figure S1: Microstructure for different doses of O-implanted Pt, (a) 2×10^{16} ions cm^{-2} , (b) 5×10^{16} ions cm^{-2} , and (c) 1×10^{17} ions cm^{-2} respectively, after removal of capping layers (MgO/Al₂O₃).

S2: Microwave power dependence of ST-FMR signal

We used a nominal power of $P_{\text{app}} = 10$ dBm (10 mW) in our ST-FMR measurements. To understand if this power is not large enough to induce nonlinear FMR in NiFe, we focused on power dependent ST-FMR measurements^{S1} by measuring V_{mix} at $f = 5$ GHz in wide range of P_{app} (1-12.58 mW). Figure S2 (a) shows V_{mix} for one of the O-implanted Pt samples exhibiting no change in ΔH and H_0 with increase in P_{app} . Further the extracted weight S and A (green and violet symbols) are plotted as function of power in Fig. S2 (b) with a linear fit (solid line). We can infer that precessing magnetization is in the linear regime at $P_{\text{app}} = 10$ dBm (10mW) (red box). Additionally, we plotted the ratio of weight S/A as a function of power and found it to be invariant in this applied power range as shown in Fig. S2 (c).

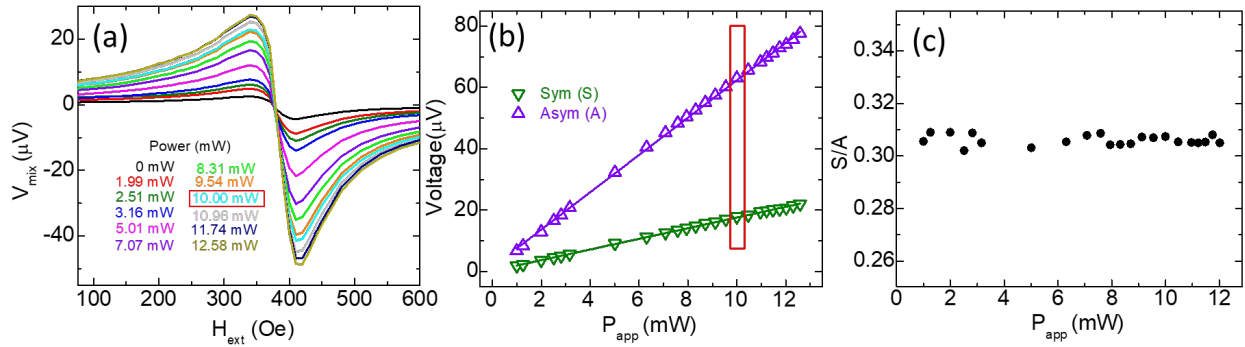


Figure S2: (a) Obtained rectified voltage spectra V_{mix} at $f = 5$ GHz for power 1-12.58 mW for one of O-implanted Pt sample. (b) Extracted S and A (with solid lines as linear fit) and (c) invariant S/A as a function of power.

S3: Role of Spin pumping contribution in the symmetric component of ST-FMR signal

The symmetric component in ST-FMR spectra has to be analyzed precisely for weak resonance signal since it might originate not only from DLT but also by spin pumping in which a precessing ferromagnet (here NiFe) pumps a spin current back into the Pt-Oxide. This spin current might get converted back to voltage output by inverse spin-to-charge conversion. Moreover, the spin pumping contribution has same $\sin 2\phi \cos \phi$ dependence and so angular dependent ST-FMR cannot be used to differentiate these two effects.

Hence, the role of spin pumping can be assessed by calculating spin pumping contribution which can be expressed as $V_{SP} = \frac{\theta_{DL}\lambda_{sd}}{d\sigma_{Pt(O)}+t\sigma_{NiFe}} \tanh\left(\frac{d}{2\lambda_{sd}}\right) \left(\frac{2e}{\hbar}\right) J_s \sin \phi$ where, θ_{DL} is DLT efficiency of Pt-Oxide, l is the length of device, λ_{sd} is spin diffusion length in the Pt-Oxide, d and $\sigma_{Pt(O)}$ are thickness and conductivity of Pt-Oxide, t and σ_{NiFe} are thickness and conductivity of NiFe, e is electronic charge, \hbar is reduced Planck constant, ϕ is the angle between external magnetic field and microwave current (45° for this case), J_s is the spin pumping current into Pt-Oxide due to precessing NiFe given as $J_s = \frac{\hbar}{2} f \sin^2 \theta_c g_{eff}^{\uparrow\downarrow}$ where, f is frequency, $g_{eff}^{\uparrow\downarrow}$ is spin mixing conductance and $\theta_c = \frac{1}{dR/d\phi} \frac{2}{I_{rf}} \sqrt{S^2 + A^2}$ in which S and A are weight factors for symmetric and antisymmetric components respectively, $dR/d\phi$ is obtained from AMR, I_{rf} is amount of current in device. For eg. V_{SP} is found to be $0.05 \mu V$ as compared to $S = 8.15 \mu V$ which is less than 1 % (~ 0.65 %) at 5 GHz for N1, V_{SP} is found to be $0.11 \mu V$ as compared to $S = 20.2 \mu V$ for N2 (~ 0.56 %) and V_{SP} is found to be $0.23 \mu V$ as compared to $S = 43.67 \mu V$ for N3 (~ 0.53 %). Therefore, spin pumping contribution does not play a significant role in our symmetric component of ST-FMR signal.

S4: Angular dependent ST-FMR measurements

The careful analysis of ST-FMR lineshape is a prerequisite to quantify the DLT as there may be latent effects such as effective field with different spin polarization, ambiguous effective field orientation, apart from the conventional spin Hall effect^{S2}. This may overlap with Symmetric and Antisymmetric signal of ST-FMR spectra. Hence, we performed angular dependent ST-FMR measurements to rule out these possibilities in our system by varying the direction of H_{ext} with respect to device length (I_{rf}) from 0° to 360° . The symmetric (S) and antisymmetric(A) components can be fitted with $\sin 2\phi \cos \phi$ where, $\sin 2\phi$ is from AMR, whereas, $\cos \phi$ is from DLT and OFT for S and A respectively.

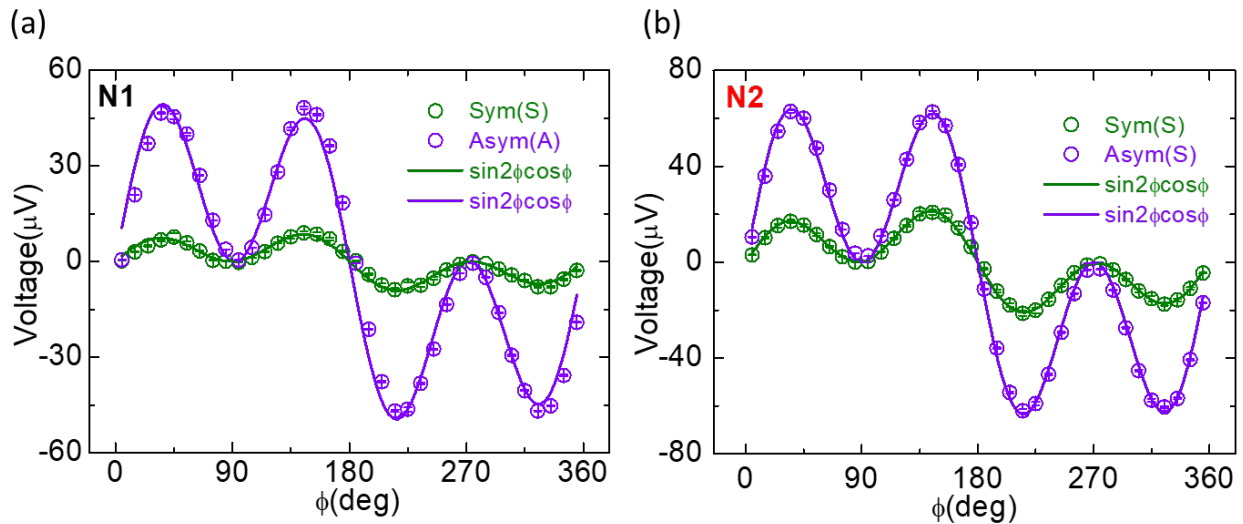


Figure S3: Angular dependence of symmetric and antisymmetric component measured at $f = 5$ GHz for a) N1 and b) N2.

S5: ST-FMR measurements for pristine Pt/NiFe

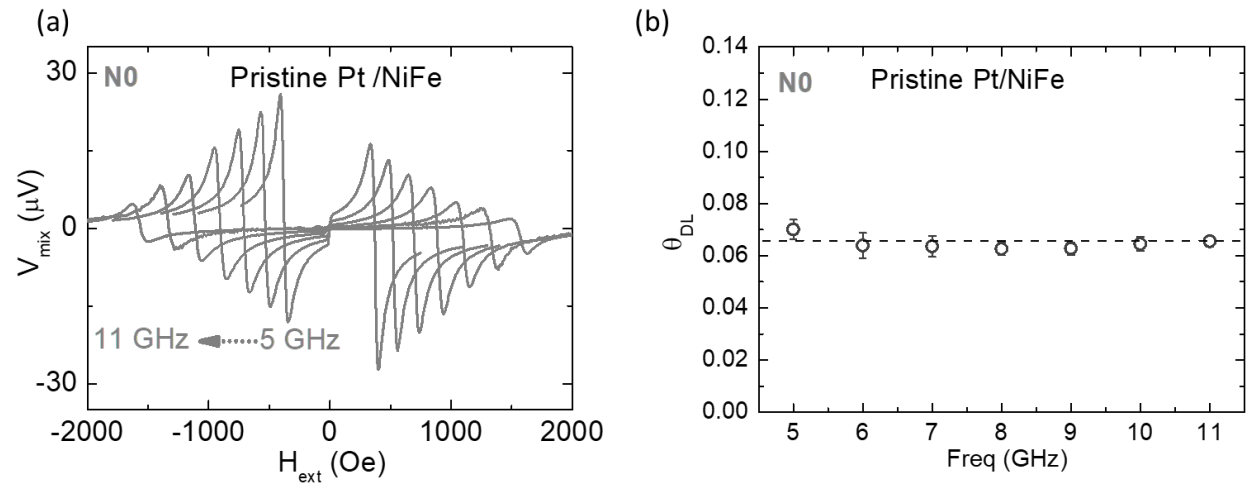


Figure S4: a) ST-FMR spectra V_{mix} and b) θ_{DL} obtained for $f = 5$ to 11 GHz for sample N0:
Pristine Pt/NiFe.

Supplemental references

- ^{S1} Y. Wang, P. Deorani, X. Qiu, J. H. Kwon, and H. Yang, *Appl. Phys. Lett.* **105**, 152412 (2014).
- ^{S2} Y. Ou, Z. Wang, C. S. Chang, H.P. Nair, H. Paik, N. Reynolds, D.C. Ralph, D. A. Muller, D. G. Schlom, and R. A. Burhman, *Nano Lett.* **19**, 3663 (2019).